# Nonintrusive High-Impedance Ground Fault Detection and Localization

Aaron W. Langham, *Member, IEEE,* Thomas C. Krause, *Member, IEEE,* Maxwell C. Buchanan, and Steven B. Leeb, *Fellow, IEEE*

***Abstract*—Ground faults are notoriously difficult to localize on ungrounded and high-resistance grounded three-phase ac power systems. These systems are designed to ride through one line-to-ground fault without tripping protective equipment. Although this strategy increases reliability, it makes single line-to-ground fault detection and localization difficult. A lengthy manual inspection is required to find the load responsible for a ground fault. This is exacerbated when faults are intermittent in nature. This work presents instrumentation and measurement techniques that turn a nonintrusive load monitor into a fault localization tool for ungrounded and high-resistance grounded systems. We show that by measuring line currents with sufficient resolution and sampling rate, a nonintrusive load monitor can extract small zero-sequence fault currents from parasitic capacitive return paths. Since measurement uncertainty is inherent to computing zero-sequence current from line currents, we develop a correction scheme. We present a method and instrumentation for both detecting and localizing single line-to-ground faults to an individual piece of equipment with a nonintrusive power monitor.**

***Index Terms*—Ground fault localization, power monitoring, ungrounded power systems**

## I. GROUNDWORK

Ground faults can damage equipment, bring down a section of a power grid, and injure personnel. Single line-to-ground (SLG) faults are among the most common power system faults, motivating advanced instrumentation and measurement for early SLG fault detection and localization [1], [2]. Three-phase power distribution topologies typically mitigate ground faults by bonding a neutral point to ground or by completely isolating line conductors from ground. Power grids with especially high resiliency requirements such as marine microgrids often use ungrounded delta-wired or high-resistance grounded (HRG) wye-wired topologies. In principle, this allows exactly one phase to be shorted to a local ground (such as a ship hull) without disrupting service or tripping protective equipment [3]. However, a subsequent ground fault on another phase will result in a much larger line-to-line fault, tripping protective equipment and bringing down the grid. Although the grid can ride through one line-to-ground fault, timely detection and localization of this fault is critical.

A. W. Langham is with The Cooper Union for the Advancement of Science and Art, New York, NY 10008 (email: aaron.langham@cooper.edu).

T. C. Krause is with Elmore Family School of Electrical and Computer Engineering, Purdue University, West Lafayette, IN 47906 USA (email: krause24@purdue.edu).

S. B. Leeb is with the Massachusetts Institute of Technology, Cambridge, MA 02139 USA (email: sbleeb@mit.edu).

M. C. Buchanan is with the United States Coast Guard, Washington, DC 20032 USA.

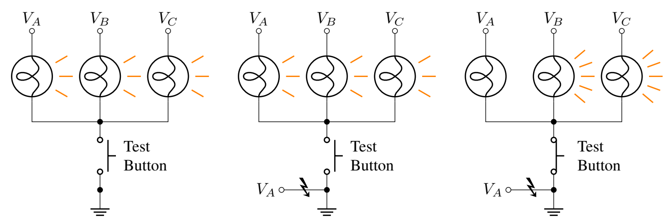


Fig. 1: Circuit schematics for a tester that uses ground fault indicator bulbs on an ungrounded power grid. The test button is closed to check for a ground fault. Left: No ground fault. Middle: One SLG fault on phase A. Right: One SLG fault on phase A with the neutral point connected to ground.

### A. Background

Single line-to-ground detection systems on ungrounded or HRG grids typically measure each line-to-ground voltage to infer fault status [4]. Legacy systems often use three identical light bulbs wired in wye with the resulting neutral point temporarily or permanently bonded to ground, as shown in Fig. 1. On a healthy system without a ground fault, line-to-neutral voltage is applied across each bulb, whether the neutral point is connected to ground or not. However, if one phase is faulted to ground, the corresponding phase's lamp will be effectively shorted out and will go dark as a result. The other two lamps will then glow brighter due to a line-to-line voltage being applied across them, rather than the smaller line-to-neutral voltage. A watchstander must periodically inspect the lamps to detect ground faults. Modern systems with voltage monitoring equipment can perform this automatically by continually measuring and digitizing each line-to-ground voltage. Alternatively, insulation monitoring systems continuously measure the impedance between each line and ground, and raise an alert if it drops too low [4].

Although modern fault detection systems automatically alert grid operators when a ground fault occurs, they typically do not explain *where* the fault occurred. Stated another way, these techniques provide ground fault *detection* but not *localization*. In general, fault localization may refer to associating a fault with a feeder, a load, or an exact point on a power system. In this work, localization refers to associating a fault with an electrical load. Once detected, a lengthy troubleshooting process ensues, where every power system branch must be disconnected to narrow down the potential fault locations [4]. Signal injection techniques can also be used to localize ground faults at the cost of requiring extra equipment and potentially needing to de-energize the system [5], [6]. Data-driven techniques such as neural networks seek to find patterns associated with faults without physical system models [6], [7], but require extensive training data and time. When faults are intermittent, the problem becomes impossible to reliably reproduce and can take weeks of maintenance work to identify and fix. Intermittent faults may be due to a ground fault on a periodically or randomly actuated loads. Accordingly, there is a clear need for automatic techniques that perform both fault detection and localization on ungrounded and high-resistance grounded systems with high reliability requirements.

Rapid ground fault localization requires correlating a ground fault indicator with the physical load actuation at the moment the indicator triggered. This is often an incompatible requirement with existing ground fault monitoring systems, whether legacy or digital. For example, a watchstander will likely notice that the monitoring bulbs have changed brightness well after the time the fault actually started. Digital systems that closely monitor ground fault indicators (such as line-to-ground voltages) may have access to programmable logic controller (PLC) switching times, making it plausible that ground faults could be correlated with load operation. However, PLC actuation and the fault occurrence may be decoupled in time. For example, actuating the PLC for a complex machine or appliance may not immediately cause faulty motors and heaters to be connected to the grid. In addition, this requires PLC sensing at *every* piece equipment, which scales poorly with complex collections of connected equipment.

There is another way. A nonintrusive load monitor (NILM) measures aggregate voltages and currents and can detect system pathologies, for example, by computing ground fault indicators and correlating these indicators in time with equipment identification using aggregate electrical data. In previous literature, indicators such as zero-sequence current magnitude and third harmonic have been used to successfully identify shipboard faults [8], [9]. The cost of the NILM's lower hardware burden than invasive techniques (such as time-domain reflectometry) is that it sees aggregate currents that need to be disaggregated into individual pieces of equipment, either manually or computationally. Electrical equipment leaves a distinct "fingerprint" event in aggregate power data. Each time the NILM observes an electrical event it performs pattern classification to identify the load responsible for the event. A NILM with line-to-ground voltage measurements can correlate ground fault indicators (such as a drop in a line-to-ground rms voltage) with load operation. When line-to-ground voltage measurements are not available, a NILM can compute high-bandwidth zero-sequence currents as another ground fault indicator.

Ground faults create unintentional return paths for fault currents, resulting in line currents that do not add up to zero. In symmetrical component theory, these are known as zero-sequence currents [10]. On ideal three-wire systems, the presence of any zero-sequence current indicates a system pathology. When a neutral point is solidly bonded to ground at the transformer or generator, large fault currents appear when a line faults to ground. However, on completely ungrounded power systems, fault currents to a chassis ground are small and require careful signal processing and sensing. For example, any imbalances in current sensors create uncertainty in computing the zero-sequence current [1], [11].

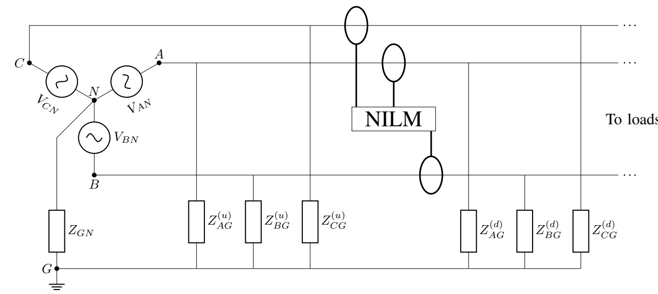


Fig. 2: Circuit schematic of a generic three-phase power system with a NILM and its impedances to ground.

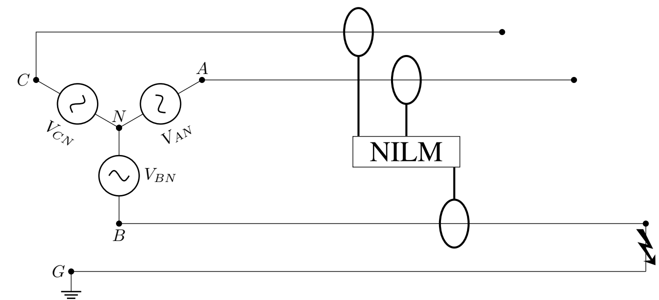


Fig. 3: Circuit schematic of an ungrounded three-phase power system one line-to-ground fault on phase B.

This paper presents circuit analysis, sensor modeling, and a shipboard microgrid case study for nonintrusive ground fault detection and localization on ungrounded systems with zero-sequence current indicators. Section II presents circuit analysis of the zero-sequence fault currents observed at a given metering point. Section III presents sensor and signal modeling to analyze the effect of gain and offset errors on zero-sequence current computation from line currents. Section IV presents real shipboard microgrid data during induced single line-to-ground faults. Finally, Section V concludes.

## II. Zero-Sequence Indicator Currents

Ground faults introduce unintentional current paths in all power systems. For example, in three-phase four-wire systems, if the sum of the currents on each phase does not equal the return current on the neutral wire, protective equipment trips. On three-wire ungrounded systems, however, fault currents "return" through small parasitic capacitances. On high resistance-grounded systems, fault currents must flow through a large impedance between the source's neutral point and ground. By design, these fault currents are kept small to avoid tripping protective equipment. This section develops a circuit model to predict fault current values seen at a metering point in an arbitrary three-wire ac power system.

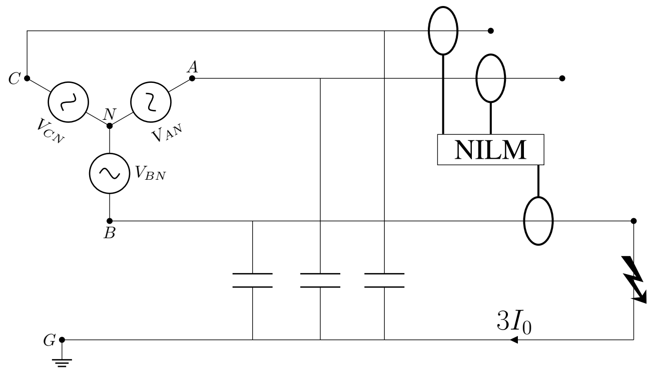


Fig. 4: Circuit schematic of an ungrounded three-phase power system with one line-to-ground fault on phase B, with capacitive zero-sequence path shown.

### A. Circuit Analysis

Fig. 2 shows a generic three-phase ac circuit model with a nonintrusive load monitor (NILM) placed at a metering point such as a subpanel. Line-to-line components of loads are present but are omitted for simplicity since they do not draw zero-sequence current. The elements of Fig. 2 model any line-to-ground coupling present in the power system, whether from loads, protective equipment, or cabling. "Ground" in this system refers to a connection (intentional or unintentional) to a chassis or common electrical plane. The NILM measures and digitizes the three line currents at the metering point. The components $Z_{AG}^{(u)}$, $Z_{BG}^{(u)}$, $Z_{CG}^{(u)}$ represent the line-to-ground impedances upstream of the monitoring point. The components $Z_{AG}^{(d)}$, $Z_{BG}^{(d)}$, $Z_{CG}^{(d)}$ represent the line-to-ground impedances downstream of the monitoring point. The component $Z_{GN}$ represents the impedance between the source's neutral point and ground. This circuit diagram generalizes to all three-wire power system grounding strategies, including:

- Solidly grounded systems: the neutral point is bonded to ground ($Z_{GN} \approx 0$) and available for single-phase load connections.
- High-resistance grounded systems: $Z_{GN}$ is large and mostly resistive.
- Low-resistance grounded systems: $Z_{GN}$ is small and mostly resistive.
- Ungrounded wye systems: the neutral point is floating ($Z_{GN} \to \infty$).
- Ungrounded delta systems: there is no neutral point ($Z_{GN} \to \infty$).
- Corner-grounded delta systems: there is no neutral point ($Z_{GN} \to \infty$) and one phase $\phi$ is bonded to ground ($Z_{\phi G} \approx 0$).

For an ideal ungrounded power system with no ground faults, all of the impedances in Fig. 2 are infinite. Fig. 3 shows the circuit diagram for an ideal ungrounded power system with phase B faulted to ground. On such an idealized system, there is no return path for fault current to flow from the ground back to the source. However, in practice, there is always some capacitance between the lines (and possibly the neutral point) and ground. For example, metallic structures near line conductors create parasitic capacitance to ground. In addition, input filters for power electronic loads may place Y capacitors between each phase and ground [12]. Fig. 4 shows a circuit diagram of an ungrounded power system with these parasitic capacitances included and phase B faulted to ground. These capacitances, which here are modeled as independent of system frequency, create a high-impedance return path that allows fault currents to flow. Also, sensors such as ground fault detection bulbs wired in wye near the source may leave their neutral point permanently bonded to ground, providing another return path for fault current.

On an ideal ungrounded power system with $Z_{GN} \to \infty$, the currents from the three voltage sources *must* sum to zero by Kirchhoff's current law. The zero-sequence current seen at the source cannot indicate whether a single line-to-ground fault has occurred. However, a NILM placed downstream of the source will also be downstream of capacitances that form a return path for the fault. At this metering point, the line currents will not sum to zero during a fault, due to the presence of the capacitive return path bypassing the metering point. As a result, single line-to-ground faults can appear in the zero-sequence currents computed by a power monitor placed downstream of the generation and upstream of a faulty load.

Applying the complex phasor form of Ohm's law to the circuit in Fig. 2 yields the following phasor-domain line currents measured by the NILM, given phasor-domain line-to-neutral and ground-to-neutral voltages:

$$I_A = \frac{V_{AN} - V_{GN}}{Z_{AG}^{(d)}}, \tag{1}$$

$$I_B = \frac{V_{BN} - V_{GN}}{Z_{BG}^{(d)}}, \tag{2}$$

$$I_C = \frac{V_{CN} - V_{GN}}{Z_{CG}^{(d)}}. \tag{3}$$

The ground-to-neutral voltage $V_{GN}$ depends on the source voltages and all of the ground-to-neutral impedances present in the system. The total line-to-ground impedance for each phase is equal to the parallel combinations of the upstream and downstream impedance:

$$Z_{AG} = Z_{AG}^{(u)} \parallel Z_{AG}^{(d)}, \tag{4}$$

$$Z_{BG} = Z_{BG}^{(u)} \parallel Z_{BG}^{(d)}, \tag{5}$$

$$Z_{CG} = Z_{CG}^{(u)} \parallel Z_{CG}^{(d)}, \tag{6}$$

where the $\parallel$ operator is defined such that $Z_1 \parallel Z_2$ yields $\left(Z_1^{-1} + Z_2^{-1}\right)^{-1}$. Evaluating Ohm's law with these total impedances to ground yields the following Kirchhoff's current law expression:

$$\frac{V_{AN} - V_{GN}}{Z_{AG}} + \frac{V_{BN} - V_{GN}}{Z_{BG}} + \frac{V_{CN} - V_{GN}}{Z_{CG}} = \frac{V_{GN}}{Z_{GN}}. \tag{7}$$

Rearranging and solving for $V_{GN}$ yields:

$$V_{GN} = \frac{\frac{V_{AN}}{Z_{AG}} + \frac{V_{BN}}{Z_{BG}} + \frac{V_{CN}}{Z_{CG}}}{\frac{1}{Z_{AG}} + \frac{1}{Z_{BG}} + \frac{1}{Z_{CG}} + \frac{1}{Z_{GN}}}. \tag{8}$$

This can also be derived using Millman's theorem [13], [14]. Summing the three currents from Eqs. (1), (2), and (3) and

TABLE I: Simulated fault currents seen at two different metering points.

| Scenario | Metering Point | $\lvert V_{GN}\rvert$ (V) | $\angle V_{GN}$ | $\lvert I_0\rvert$ (mA) | $\angle I_0$ |
|---|---|---|---|---|---|
| A SLG | Switchboard | 259.8 | $0°$ | 9.8 | $90°$ |
| B SLG | Switchboard | 259.8 | $-120°$ | 9.8 | $-30°$ |
| C SLG | Switchboard | 259.8 | $120°$ | 9.8 | $-150°$ |
| A SLG | Distribution | 259.8 | $0°$ | 107.7 | $90°$ |
| B SLG | Distribution | 259.8 | $-120°$ | 107.7 | $-30°$ |
| C SLG | Distribution | 259.8 | $120°$ | 107.7 | $-150°$ |

TABLE II: Simulated zero-sequence currents for SLG faults both upstream and downstream of the metering point.

| Scenario | $\lvert V_{GN}\rvert$ (V) | $\angle V_{GN}$ | $\lvert I_0\rvert$ (mA) | $\angle I_0$ |
|---|---|---|---|---|
| No Fault | 0 | - | 0 | - |
| A SLG Upstream | 259.8 | $0°$ | 0.98 | $-90°$ |
| B SLG Upstream | 259.8 | $-120°$ | 0.98 | $150°$ |
| C SLG Upstream | 259.8 | $120°$ | 0.98 | $30°$ |
| A SLG Downstream | 259.8 | $0°$ | 9.8 | $90°$ |
| B SLG Downstream | 259.8 | $-120°$ | 9.8 | $-30°$ |
| C SLG Downstream | 259.8 | $120°$ | 9.8 | $-150°$ |

dividing by three yields $I_0$, the phasor-domain zero-sequence current seen by the NILM:

$$I_0 = \frac{V_{AN} - V_{GN}}{3Z_{AG}^{(d)}} + \frac{V_{BN} - V_{GN}}{3Z_{BG}^{(d)}} + \frac{V_{CN} - V_{GN}}{3Z_{CG}^{(d)}}. \quad (9)$$

Together, Eqs. (8) and (9) describe the zero-sequence current measured at a metering point, given the upstream and downstream line-to-ground impedances.

### B. Metering Point Placement

The fault current seen by a metering point is governed by Eqs. (8) and (9), which in turn depend on the values of $Z_{\phi G}^{(u)}$ and $Z_{\phi G}^{(d)}$ for each phase $\phi$. These upstream and downstream line-to-ground impedances are governed by where the metering point is placed in the power system. Longer cable runs, for example, create larger line-to-ground capacitances. Consider a power system with two candidate metering points: one at a main switchboard with $C_{\phi G}^{(u)} = 100\text{nF}$ and $C_{\phi G}^{(d)} = 1\mu\text{F}$, and one at a distribution panel with $C_{\phi G}^{(u)} = 1.1\mu\text{F}$ and $C_{\phi G}^{(d)} = 1\text{nF}$, for each phase $\phi$. In both cases, this system is faulted to ground through a $1\Omega$ resistor downstream of the metering point, for each phase. Table I shows the resulting zero-sequence current phasor values for both metering point placements (given as the rms value and angle in degrees), assuming a balanced 450V (rms, line-to-line) source. For both metering points, the angle of $I_0$ is the same for a given phase-to-ground fault. However, the rms value of $I_0$ is orders of magnitude smaller at the switchboard metering point than it is at the distribution point. This discrepancy is due to the lower impedance return path formed by the $100\text{nF}$ and $1\mu\text{F}$ line-to-ground capacitances seen upstream of the distribution metering point, compared to the the $100\text{nF}$ line-to-ground return path seen upstream of the switchboard metering point.

This analysis suggests that the further downstream a NILM is placed, the more successful it will be at seeing zero-sequence fault currents. In one degenerate case, a NILM placed directly at a single load will have the most favorable return path for fault currents, but only be able to see one load. In the other case, a NILM placed directly at an ungrounded generator will see every single load's power consumption, but no fault current. This analysis reveals a new design tension between the number of visible loads, and the size of fault currents.

### C. Upstream and Downstream Faults

The observed fault current is governed by the ground-to-neutral voltage and line-to-ground impedances. Both of these change whenever there is an SLG fault in the system, regardless of whether it is upstream or downstream of the metering point. In principle, this means that both upstream and downstream SLG faults could be seen in the zero-sequence current at the metering point. However, the actual values of the zero-sequence fault current for both situations depend heavily on the relative sizes of the upstream and downstream impedances to ground. Table II shows the results of simulating the zero-sequence current $I_0$ measured by the metering point in Fig. 2 for several line-to-ground fault conditions. In the "No Fault" scenario, a balanced set of three $100\text{nF}$ capacitances comprised the upstream line-to-ground impedances and a balanced set of $10\text{nF}$ capacitances comprised the downstream phase-to-ground impedances. The ground-to-neutral impedance $Z_{GN}$ was set to a capacitance of $10^{-20}\text{F}$, effectively an open circuit. In the faulted scenarios, a $1\Omega$ resistor was added in parallel with the corresponding upstream or downstream capacitance. Although $V_{GN}$ is the same for both upstream and downstream faults, the corresponding zero-sequence current phasors differ in magnitude by a factor of ten due to the relative size difference of the different upstream and downstream capacitances. In addition, the phase angles of the upstream faults and the corresponding downstream faults are flipped in sign.

## III. Sensor and Signal Models

Accurately measuring zero-sequence current on ungrounded systems requires careful consideration of imbalances in the measurement system. On high-impedance grounded systems, the zero-sequence current can simply be measured directly through the ground-to-neutral impedance. However, on systems without a neutral current to measure, such as ungrounded delta systems, measuring zero-sequence current without specialized zero-sequence transformers must be done by summing all three line current measurements. This is problematic, however, because current measurement equipment must be sized for each line current (tens to hundreds of amps), and yet the ultimate quantity of interest is relatively minuscule (milliamps).

### A. Measurement Uncertainty

Practical current transducers and data acquisition hardware always have nonidealities. These may include nonlinearities,

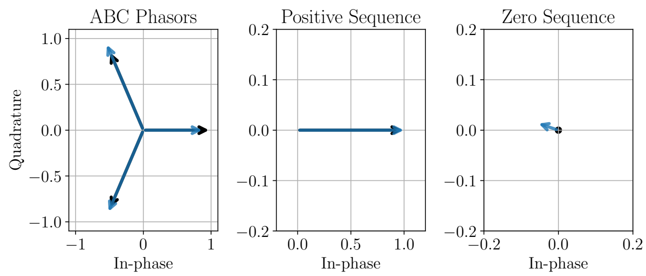


Fig. 5: Normalized current phasors in the ABC, positive, and zero-sequence domains. An ideal balanced set is shown in black, and the resulting measured phasors with current sensor gains of 0.9, 1.1, and 1.05 are shown in blue.

thermal noise, and poorly characterized gains and offsets. All of these nonidealities result in imperfect reconstructions of zero-sequence current when summing the three phase currents [11].

Consider a current sensor and data acquisition pipeline that measures the instantaneous current on phase $\phi$, $i_\phi(t)$, and records $\hat{i}_\phi(t)$. Denoting the measurement error between $i_\phi(t)$ and $\hat{i}_\phi(t)$ as $\epsilon_\phi(t)$ yields the following:

$$\hat{i}_\phi(t) = i_\phi(t) + \epsilon_\phi(t). \tag{10}$$

In magnetic current transformers, for example, part of the error is often given as a proportion of the measured current. This is often referred to as "gain error" [15], [16]. In addition, "offset error" is a constant error component independent of the measured current. Gain and offset error also appear from nonidealities in filters, amplifiers, and analog-to-digital converters in the signal processing chain of any measurement device. The total gain error as a proportion of measured current can be denoted as $k_\phi$, and the offset error is denoted here as $m_\phi$. These specific parameter values belong to a specific device and setup, rather than being general across current measurement equipment, yielding the following expression for $\hat{i}_\phi(t)$:

$$\hat{i}_\phi(t) = i_\phi(t) + k_\phi i_\phi(t) + m_\phi = (1 + k_\phi)i_\phi(t) + m_\phi. \tag{11}$$

For an ideal device, $k_\phi = 0$ and $m_\phi = 0$. The continuous-time signal $\hat{i}_\phi(t)$ is sampled, producing the discrete-time sequence $\hat{i}_\phi[n]$. For each voltage waveform period on phase $\phi$, an estimate of the instantaneous phasor current can be obtained via the discrete Fourier transform (DFT). By evaluating the DFT at the line frequency, harmonics from distortion or nonlinear loads are rejected. Denoting the number of samples per waveform period as $N$, the following equations produce the in-phase and quadrature components of the estimated current phasor $\hat{I}_\phi = \hat{I}_\phi^{(i)} + j\hat{I}_\phi^{(q)}$:

$$\hat{I}_\phi^{(i)} = \frac{1}{N}\sum_{n=0}^{N-1} \hat{i}_\phi[n]\cos(2\pi n/N), \tag{12}$$

$$\hat{I}_\phi^{(q)} = \frac{1}{N}\sum_{n=0}^{N-1} \hat{i}_\phi[n]\sin(2\pi n/N). \tag{13}$$

Substituting the value of $\hat{i}_\phi$ from Eq. (11) and splitting the sums into to parts allows the DFT to be computed separately for both the $(1+k_\phi)i_\phi(t)$ and $m_\phi$ parts. Since $m_\phi$ is constant, its contributions to $\hat{I}_\phi^{(i)}$ and $\hat{I}_\phi^{(q)}$ will be zero. Defining the phasor current estimate made with perfect measurements of $i_\phi(t)$ as $I_\phi = I_\phi^{(i)} + jI_\phi^{(q)}$ yields the following:

$$\hat{I}_\phi^{(i)} = \frac{1 + k_\phi}{N}\sum_{n=0}^{N-1} i_\phi[n]\cos(2\pi n/N) = (1 + k_\phi)I_\phi^{(i)}, \tag{14}$$

$$\hat{I}_\phi^{(q)} = \frac{1 + k_\phi}{N}\sum_{n=0}^{N-1} i_\phi[n]\sin(2\pi n/N) = (1 + k_\phi)I_\phi^{(q)}. \tag{15}$$

These equations show that for a current measurement system with both gain and offset errors, the offset error does not affect the estimated phasor $\hat{I}_\phi$. Instead, gain errors in waveform measurements propagate to the phasor estimate $\hat{I}_\phi = (1 + k_\phi)I_\phi$.

### B. Gain Error Artifacts

Adding $\hat{I}_A$, $\hat{I}_B$, and $\hat{I}_C$ and dividing by three yields the zero-sequence current phasor estimate $\hat{I}_0$. Denoting the zero-sequence current phasor estimate obtained without measurement error as $I_0 = (I_A + I_B + I_C)/3$ yields the following:

$$\hat{I}_0 = \frac{\hat{I}_A + \hat{I}_B + \hat{I}_C}{3} = \frac{k_A I_A + k_B I_B + k_C I_C}{3} + I_0. \tag{16}$$

Even if the true zero-sequence current is zero, the estimated zero-sequence current may be nonzero if $k_A$, $k_B$, and $k_C$ are not equal. Although $k_\phi$ may be smaller than 1% [17], it is multiplied by the large phase currents $I_A$, $I_B$, and $I_C$. As such, it can create a sizable artifact on the same order of magnitude as the small zero-sequence current from SLG faults.

Although the gain error in line current measurement may be negligible when computing positive-sequence power flow, this has an outsize impact on the zero-sequence current. Fig. 5 shows an example of this for $k_A = 0.9$, $k_B = 1.1$, and $k_C = 1.05$. Effectively, the mismatch in sensor gains causes positive-sequence current to "leak" into the zero-sequence current estimate. For example, consider a balanced set of 5 A (rms) currents monitored by sensors with $k_A = 0.99$, $k_B = 1.01$, and $k_C = 1$. Since the line currents are balanced, the true value of $I_0$ is zero. However, the zero-sequence current estimate using Eq. (16) results in an $\hat{I}_0$ of approximately 28.9 mA rms. This artifact confounds fault detection, since it is on the order of magnitude as the values of $I_0$ predicted in Tables I and II. Smaller load currents produce smaller zero-sequence artifacts. For example, the motor in Section IV-A draws approximately 0.47 A rms per-phase. With current sensor gains of 0.99, 1.01, and 1, this load produces an $\hat{I}_0$ of approximately 2.7 mA rms. This is appreciably smaller than the "Downstream" and "Distribution" fault currents in Tables I and II.

Inferring the exact values of $k_\phi$ for each phase $\phi$ requires a known current $I_\phi$ and the resulting measured current $\hat{I}_\phi$. These values can be combined with least-squares optimization and Eq. (11) to produce an estimate for $k_\phi$. However, this is not particularly practical, especially on retrofit installations

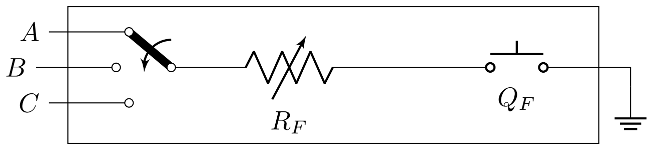


(a) Circuit diagram.

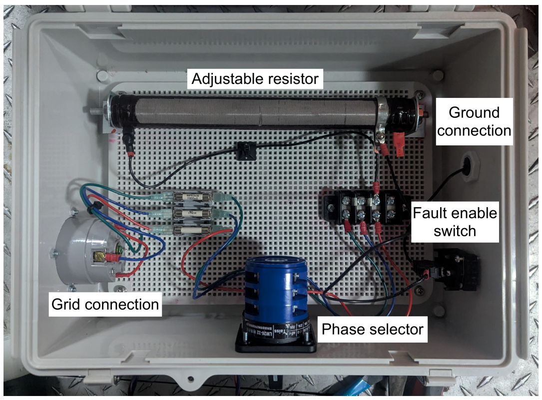


(b) Implementation.

Fig. 6: Ground fault emulator instrumentation.

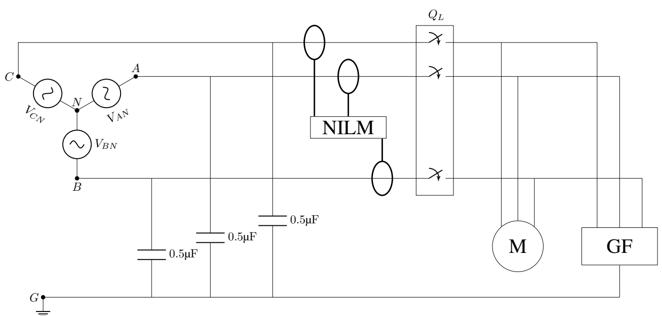


Fig. 7: Circuit schematic for the ungrounded lab experiment in Section IV-A.

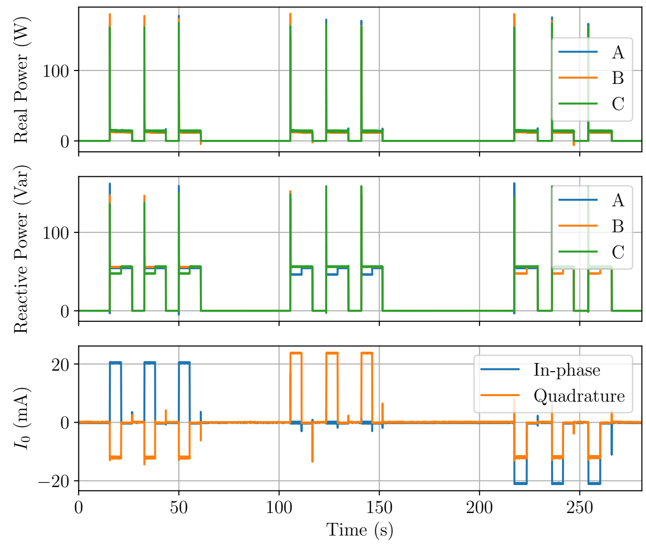


Fig. 8: Three motor turn-on events with simultaneous single line-to-ground faults, for each phase.

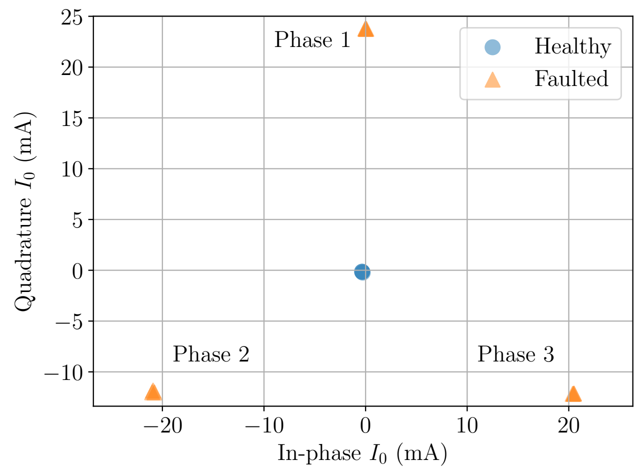


Fig. 9: Steady-state difference in zero-sequence current phasor for both healthy and faulted motor runs.

where exact load current values are unknown and invasive system identification methods may be unworkable. Instead, a NILM can "learn" how to compensate for zero-sequence artifacts such as these, provided they have two properties. First, they must be repeatable. This means that for the same load event, the same zero-sequence artifact must appear. Second, the artifact zero-sequence current must be proportional to the actual line currents. This means that a baseline "normal" value of $\hat{I}_0$ can be characterized for all loads of interest. Denoting the baseline zero-sequence measurement for a load as $\hat{I}_0^{(b)}$, future measurements of the load's zero-sequence current can be corrected by subtracting the baseline from the measured $\hat{I}_0$:

$$\hat{I}_0 = \frac{\hat{I}_A + \hat{I}_B + \hat{I}_C}{3} - \hat{I}_0^{(b)}. \tag{17}$$

The magnitude of this "corrected" $\hat{I}_0$ indicates whether a fault is present. The most basic fault detection strategy involves setting a threshold on the value of $|\hat{I}_0|$ to be considered healthy. However, pattern classification and machine learning techniques of any complexity can use the in-phase and quadrature components of $\hat{I}_0$ as input features for ground fault detection.

Importantly, the baseline correction term $\hat{I}_0^{(b)}$ is specific to an individual NILM installation. For permanent NILM installations, each load's baseline can be reused over time, as long as the measurement equipment is undisturbed and sensor gains do not change over time. However, whenever current sensors are installed or reinstalled, a new baseline should be characterized for each load. If the gains of the current transducers change over time, due to large temperature changes or sensor degradation, the baseline will need to be periodically recomputed.

## IV. Instrumentation Demonstration

A practical implementation of a nonintrusive fault localization scheme requires an understanding of what values of $\hat{I}_0$ are pathological. Instrumentation presented here emulates a single line-to-ground fault on a chosen phase, actuating at the same time as a chosen piece of equipment. Fig. 6 shows

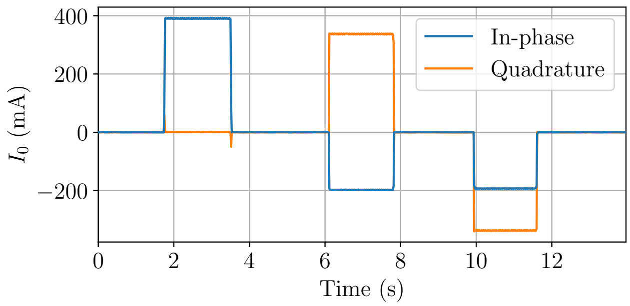


Fig. 10: SLG faults through an approximately $250\Omega$ resistor while the ship power system was solidly grounded.

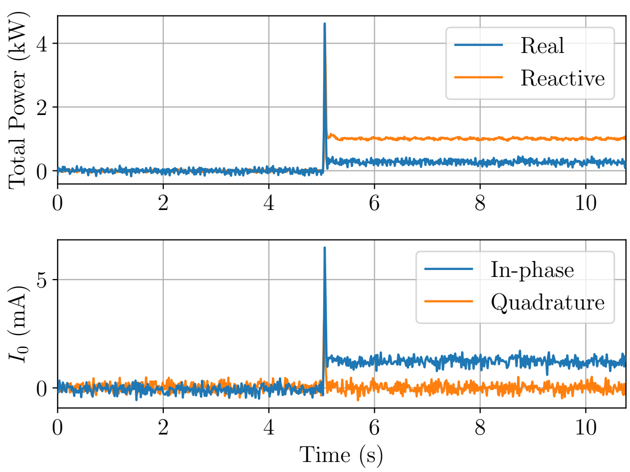


Fig. 11: Zero-sequence current artifact from a shipboard oil pump energizing at $t = 5s$.

the circuit schematic and implementation picture for a ground fault emulation instrument. An adjustable power resistor is connected between a chosen phase and ground when the switch $Q_F$ is closed. When this is wired downstream of a load's control circuitry, as shown in Fig. 7, it will produce a ground fault at the exact instant the load is powered on. This produces a distinct signature that an upstream power monitor can recognize and learn. This section presents two demonstrations of ground fault characterization and localization instrumentation. The first experiment uses a laboratory setup with known discrete capacitances to ground. The second experiment uses a real shipboard microgrid on US Coast Guard Cutter *Sturgeon*, an 87-foot patrol boat homeported in Boston, MA at the time of the experiment.

The measurement system presented here computes power spectral envelopes from currents and voltages sampled at $8\text{kHz}$ with a 16-bit ADC. The nominal voltage waveform frequency in these experiments is $60\text{Hz}$. Each spectral envelope computation window is aligned to one period of the voltage waveform, even if it deviates from the nominal frequency.

### *A. Lab Experiment*

To validate the simulation and circuit analysis presented in Section II, experiments were performed with known discrete $0.5\mu\text{F}$ capacitances from each phase to ground. Fig. 7 shows a circuit schematic. An isolated three-phase power supply with a floating neutral point served as the generation source, emulating an ungrounded power system. A nonintrusive load monitor was configured downstream of the discrete $0.5\mu\text{F}$ capacitors. Downstream of the NILM, a three-phase induction machine was connected. In addition, the ground fault emulation instrument from Fig. 6 was connected between the motor and its controller.

Applying Eqs. (8) and (9) for a $1\Omega$ fault to ground on any phase results in a predicted rms fault current of $22.7\text{mA}$. Both the induction machine and the ground fault emulator were downstream of a three-pole, single throw switch standing in for a motor controller. This setup emulates a load turning on with a ground fault condition, which may clear before the load turns off. The test procedure involved holding the normally open switch $Q_F$ closed and then closing the three-pole, single-throw switch $Q_L$. The NILM sampled the current and voltage waveforms at 8 kHz and generated fundamental real and reactive power spectral envelopes at the grid frequency (60 Hz) for each phase. When scaled properly, these spectral envelopes can be interpreted as instantaneous measurements of the line current phasors. Summing these line current phasors and dividing by three yields an instantaneous estimate of the zero-sequence current phasor. Fig. 8 shows the real and reactive power signatures and zero-sequence current phasor values from performing this three times for each phase. For each phase, the steady-state rms zero-sequence current is approximately $23.7\text{mA}$. The angles of each phase's zero-sequence fault current collectively form a balanced three-phase set. This can be seen graphically in Fig. 9, which shows the steady-state difference in the in-phase and quadrature components of the zero-sequence current phasor for both healthy (blue circle) and faulted conditions (orange triangle). The angles of the fault currents ($90°$, $-150°$, and $-30°$) match those predicted for the downstream faults in Table II.

### *B. Shipboard Microgrid Experiment*

As a starting point for characterizing SLG fault currents on this system, three single line-to-ground faults were emulated while the ship was connected to shore power. When connected to shore power, this ship's power system is effectively a solidly grounded three-wire power system with approximately 277 V rms from each line to ground. As the first experimental test condition, the value of $R_F$ in the ground fault box was set to approximately $250\Omega$ rather than a dead short, so that protective equipment would not trip. This emulates a high-resistance fault from one line to ground. Fig. 10 shows the resulting zero-sequence current phasors seen from faulting each line sequentially to ground through $R_F$. Since the system's neutral point is solidly grounded, the full line-to-neutral voltage appears across the fault resistance, resulting in a large zero-sequence current. The large fault currents seen here are orders of magnitude larger than any sensor artifacts, and they form a balanced three-phase set centered at zero. However, this solidly grounded configuration is not typical for shipboard microgrids while the ship is underway and can benefit the most from ground fault localization.

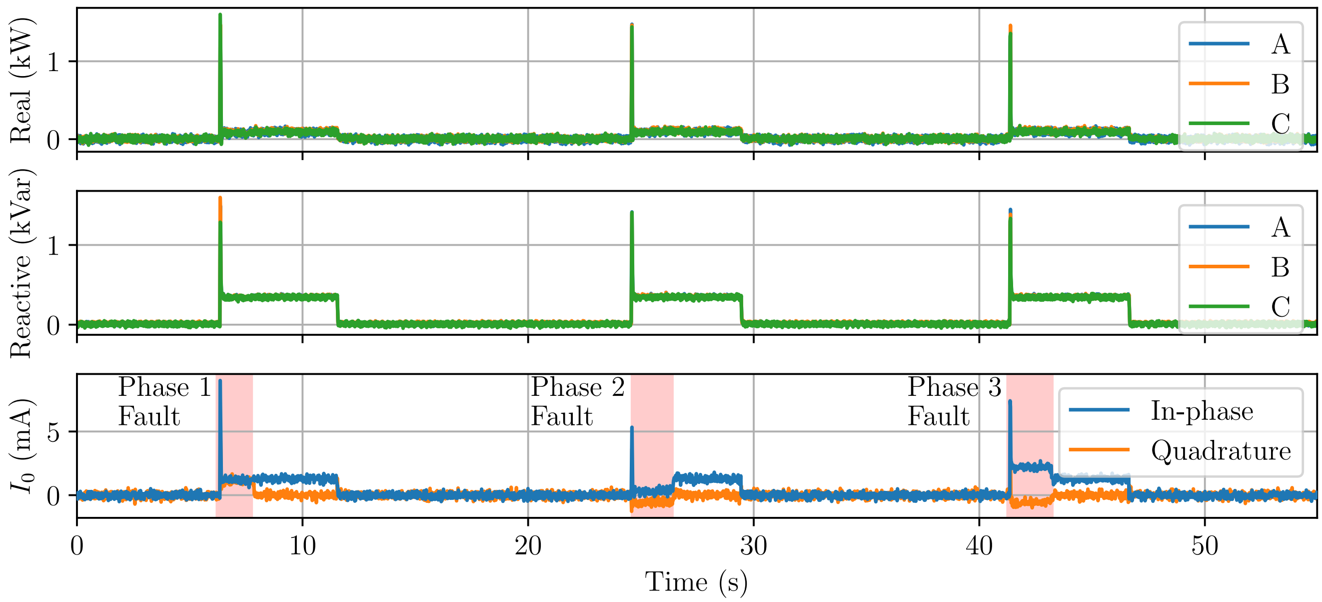


Fig. 12: Shipboard dirty oil pump runs with a single line-to-ground fault for each phase.

As a more practical experimental setup, the ship's power system was switched to an onboard generator, forming an ungrounded delta system. To emulate a load turning on with a ground fault, the ground fault box in Fig. 6 was wired in parallel with a grid-connected induction machine driving a dirty oil pump. First, a baseline zero-sequence current for the machine was measured for the pump without the ground fault. Fig. 11 shows the total real and reactive power while energizing the pump, and the measured zero-sequence current phasor over this time. The mean value of the first five samples of each of these quantities is subtracted from the stream so that they all start at zero. The inrush and general shape of the turn-on transient clearly shows up in the zero-sequence stream, likely due to sensor gain error mismatches. At steady state, the real component of this artifact is approximately $1.4\text{mA}$, and the reactive component is approximately zero.

Next, the pump was energized three times, each time with a different phase faulted directly to ground. The switch $Q_F$ was closed before energizing the load, and then released seconds before de-energizing the load. This emulates a fault condition where the load energizes with an SLG fault that clears before the load turns off. Fig. 12 shows the real and reactive power during these three pump runs in the top plots, and the corresponding zero-sequence current phasor in the bottom plot. The mean value of each quantity over the first five samples was subtracted to remove the baseline from other energized loads. Although the total real and reactive power traces for each pump run appear the same, a completely different zero-sequence current signature is seen for each pump run. For example, in the second run, there is hardly any steady-state change in in-phase zero-sequence current while the fault is active. This is due to the superposition of the zero-sequence current artifact of $1.4\text{mA}$ with the in-phase and quadrature zero-sequence fault current, whose phase depends on which line is faulted to ground.

Each phase-to-ground fault condition was recorded five times, in addition to several healthy pump runs. For each run, the steady-state difference in zero-sequence current was computed and plotted in Fig. 13. Similar to simulation and lab experiment results, the three faulted zero-sequence currents form a balanced three-phase set. However, this set is not centered around the origin, but is instead centered around the baseline zero-sequence current of approximately $1.4\text{mA}$. The healthy pump runs (shown as blue circles) were collected from two days of shipboard power data, separated by three months, showing that the zero-sequence baseline remained constant for this load over time. The measurement uncertainty of this baseline zero-sequence measurement, reported as the standard deviations of the in-phase and quadrature components, is $0.134\text{mA}$ and $0.116\text{mA}$, respectively. The translucent blue circle in Fig. 13 shows a decision boundary for separating faulty and healthy conditions. Any load runs with more than $0.4\text{mA}$ (three standard deviations of the in-phase component) in magnitude away from $\hat{I}_0^{(b)}$ are considered to exhibit a ground fault, and are shown as orange triangles. Assuming that healthy runs appear as an isotropic normal distribution centered at $\hat{I}_0^{(b)}$ with standard deviation $\sigma$, the user can set the detection threshold to be a multiple of $\sigma$ corresponding to target true positive and false positive rates. Alternatively, on power systems that log an alarm when a ground fault occurs, a user can investigate the load events around the alarm time and find the load with the most anomalous step change in zero-sequence current.

### C. Measurement and Localization

A nonintrusive power monitor can communicate diagnostic information to a crew using a timeline of load actuations and a dashboard of load statistics [18]. Fig. 14 shows an

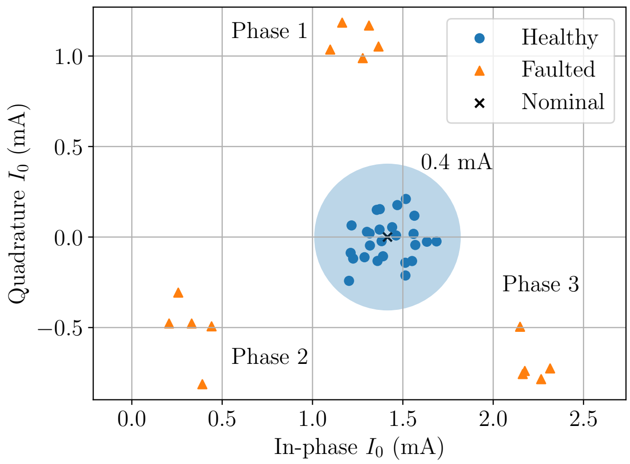


Fig. 13: Steady-state difference in zero-sequence current phasor for both healthy and faulted pump runs.

(a) Custom power monitoring box running the fault timeline prototype.

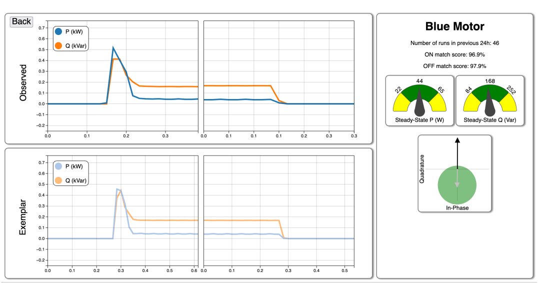


(b) Load actuation view.

Fig. 14: Interactive timeline prototype for nonintrusively locating ground faults.

interactive timeline prototype for flagging ground faults with a nonintrusive power monitor. Load actuations (periods of time when a load is operating) are encoded as bars with a start and stop time, and the health of the load is encoded with color. Clicking or tapping a load actuation bar in Fig. 14a shows the “turn-on” and “turn-off” transients associated with the both the selected load actuation and a known healthy “exemplar” actuation, as illustrated in Fig. 14b. Statistics such as number of runs, steady-state power, and zero-sequence current signature allow an operator to investigate the health of a load for any actuation.

## V. Conclusion

Ground faults on ungrounded and high impedance-grounded power systems challenge measurement systems for fault detection and localization. The instrumentation, measurement analysis, and experiments presented in this paper provide avenues for nonintrusive ground fault localization with zero-sequence currents. Three findings are summarized as follows.

First, success in finding fault currents depends on having a base understanding of system topology and impedances to ground. This informs metering point placement, and how both upstream and downstream faults appear in the observed zero-sequence currents. Instrumentation such as the ground fault emulator presented here can provide empirical characterizations of how these impedances to ground affect fault currents.

Second, on healthy ungrounded systems with practical sensing, benign step changes in zero-sequence currents show up from sensor artifacts associated with healthy load operation. This complicates fault detection when simply measuring zero-sequence current values, as it appears as if faults are constantly occurring. Instead, it may be more practical to perform load identification first, and *then* check whether the zero-sequence signature matches known values. Although this does not localize faults the instant they first occur, this does concretely link them to a load state change.

Third, gain mismatches in current measurement hardware can be corrected using a baseline in-phase and quadrature zero-sequence current associated with healthy operation, for each load. This baseline current may be on the same order of magnitude as actual fault currents, complicating fault detection and localization. Future load measurements can subtract this baseline to check whether a ground fault appears when a load energizes.

The ability of the proposed method to scale to larger systems depends in part on the measurement equipment’s ability to resolve minute changes in zero sequence current. This resolution is governed not only by the bit depth and noise of the data acquisition chain, but also by the metering placement on the power system. Extensions to this work may characterize this numerically to provide a design guide to nonintrusive meter placement on a given power system.

## Acknowledgments

The authors gratefully acknowledge the US Coast Guard and in particular the crew of the USCGC *Sturgeon*. This work was made possible through the generous support the Office of Naval Research NEPTUNE program and the inspired leadership of Dr. Scott Higgins, Dr. Corey Love, and Maria Medeiros under Research Grant N00014-24-1-2484. This work was also supported by the Landsman Foundation.

## References

[1] M.-F. Guo, H. Lin, J. Lin, and Q. Hong, “Synthetic zero-sequence signal-based intelligent location method for single-phase ground fault in distribution networks,” *IEEE Transactions on Instrumentation and Measurement*, vol. 74, pp. 1–13, 2025.

[2] J. Lin, M. Guo, and Z. Zheng, "Active location method for single-line-to-ground fault of flexible grounding distribution networks," *IEEE Transactions on Instrumentation and Measurement*, vol. 72, pp. 1–12, 2023.

[3] K.-T. Ryu and Y.-H. Lee, "Ground-fault recognition in low-voltage ships based on variation analysis of phase-to-ground voltage and neutral-point voltage," *IEEE Access*, vol. 12, pp. 123 166–123 176, 2024.

[4] N. Doerry, M. M. Islam, and J. Prousalidis, *System Grounding: Shipboard Ungrounded AC Systems (No Greater than 1 kV)*. John Wiley & Sons, Inc., 2025, pp. 15–53.

[5] T. Baldwin, F. Renovich, L. Saunders, and D. Lubkeman, "Fault locating in ungrounded and high-resistance grounded systems," *IEEE Transactions on Industry Applications*, vol. 37, no. 4, pp. 1152–1159, 2001.

[6] C. M. Furse, M. Kafal, R. Razzaghi, and Y.-J. Shin, "Fault diagnosis for electrical systems and power networks: A review," *IEEE Sensors Journal*, vol. 21, no. 2, pp. 888–906, 2021.

[7] W. Li, A. Monti, and F. Ponci, "Fault detection and classification in medium voltage dc shipboard power systems with wavelets and artificial neural networks," *IEEE Transactions on Instrumentation and Measurement*, vol. 63, no. 11, pp. 2651–2665, 2014.

[8] D. H. Green, D. W. Quinn, S. Madden, P. A. Lindahl, and S. B. Leeb, "Nonintrusive measurements for detecting progressive equipment faults," *IEEE Transactions on Instrumentation and Measurement*, vol. 71, pp. 1–12, 2022.

[9] A. W. Langham, T. C. Krause, and S. B. Leeb, "Derived power streams for fault detection and condition-based maintenance," *IEEE Access*, vol. 13, pp. 69 051–69 061, 2025.

[10] J. L. Kirtley, "System analysis and protection," in *Electric Power Principles*. John Wiley & Sons, Ltd, 2020, ch. 10, pp. 181–211.

[11] S. Nauta and R. Serra, "Zero-sequence current measurement uncertainty in three-phase power systems during normal operation," *IET Generation, Transmission & Distribution*, vol. 15, no. 24, pp. 3450–3458, 2021.

[12] R. B. Keller, *Filtering*. Cham: Springer International Publishing, 2023, pp. 245–263.

[13] J. Millman, "A useful network theorem," *Proceedings of the IRE*, vol. 28, no. 9, pp. 413–417, 1940.

[14] J. Prousalidis, "Analysis of unbalanced fault operating conditions of ship electric networks via Millman's theorem," *Journal of Marine Engineering & Technology*, vol. 21, no. 6, pp. 324–333, 2022.

[15] D. V. Retianza, J. van Duivenbode, and H. Huisman, "Plant-independent current sensor gain error compensation for highly dynamic drives," *IEEE Transactions on Industrial Electronics*, vol. 70, no. 10, pp. 9948–9958, 2023.

[16] M. C. Harke and R. D. Lorenz, "The spatial effect and compensation of current sensor differential gains for three-phase three-wire systems," *IEEE Transactions on Industry Applications*, vol. 44, no. 4, pp. 1181–1189, 2008.

[17] LEM International SA, "Current transducer LF 305-S/SP16," https://www.lem.com/sites/default/files/products_datasheets/lf_305-s_sp16.pdf, Aug. 2023, accessed: 2025-10-14.

[18] D. Green, T. Kane, S. Kidwell, P. Lindahl, J. Donnal, and S. Leeb, "NILM dashboard: Actionable feedback for condition-based maintenance," *IEEE Instrumentation & Measurement Magazine*, vol. 23, no. 5, pp. 3–10, 2020.

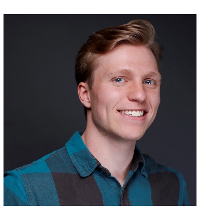

**Aaron W. Langham** (Member, IEEE) received the B.E.E. degree in electrical engineering from Auburn University, Auburn, AL, USA in 2018, and the M.S., E.E., and Ph.D. degrees in electrical engineering and computer science from the Massachusetts Institute of Technology, Cambridge, MA, USA in 2022, 2024, and 2026, respectively. He is currently an Assistant Professor at The Cooper Union for the Advancement of Science and Art in New York, NY. His research interests include signal processing, machine learning, and IoT platforms for energy systems.

**Thomas C. Krause** (Member, IEEE) received the B.S. degree in electrical engineering from Purdue University, West Lafayette, IN, USA, in 2019, and the M.S., E.E., and Ph.D. degrees in electrical engineering and computer science from the Massachusetts Institute of Technology, Cambridge, MA, USA, in 2021, 2024, and 2026 respectively. He is currently an Assistant Professor in the Elmore Family School of Electrical and Computer Engineering at Purdue University.


**Maxwell C. Buchanan** graduated from the United States Coast Guard Academy with a Bachelor's of Science in Naval Architecture and Marine Engineering in 2021. After graduation, he served as the Damage Control Assistant onboard USCGC ALEX HALEY (WMEC 39), homeported in Kodiak, AK. LT Buchanan graduated with a Master's of Science in Naval Architecture and Marine Engineering at the Massachusetts Institute of Technology in 2025 and is now a staff engineer at the USCG Marine Safety Center.

**Steven B. Leeb** received the Ph.D. degree from the Massachusetts Institute of Technology, in 1993. Since 1993, he has been a member on the MIT Faculty with the Department of Electrical Engineering and Computer Science. He also holds a joint appointment with the Department of Mechanical Engineering, MIT. He is concerned with the development of signal processing algorithms for energy and real-time control applications.